

1 Dynamic scaling of the generalized complementary relationship (GCR) improves long-term
2 tendency estimates in land evaporation

3

4 Jozsef Szilagyi^{1,2}, Richard Crago³, Ning Ma⁴

5 *¹Department of Hydraulic and Water Resources Engineering, Budapest University of
6 Technology, Budapest, Hungary, ORCID id: 0000-0003-4449-0470, Email: jszilagyil@unl.edu
7 (Corresponding author)*

8 *²Conservation and Survey Division, School of Natural Resources, University of Nebraska-
9 Lincoln, Lincoln, Nebraska, USA*

10 *³Department of Civil and Environmental Engineering, Bucknell University, Lewisburg,
11 Pennsylvania, USA*

12 *⁴Key Laboratory of Water Cycle and Related Land Surface Processes, Institute of Geographic
13 Sciences and Natural Resources Research, Chinese Academy of Sciences, Beijing, China*

14

15 **Abstract**

16 Most large-scale evapotranspiration (ET) estimation methods require detailed information of
17 land use, land cover, and/or soil type on top of various atmospheric measurements. The
18 complementary relationship of evaporation (CR) takes advantage of the inherent dynamic
19 feedback mechanisms found in the soil-vegetation-atmosphere interface for its estimation of ET
20 rates without the need of such bio-geo-physical data. Evapotranspiration estimates over the
21 conterminous United States by a new, globally calibrated, static scaling (GCR-stat) of the

22 generalized complementary relationship (GCR) of evaporation were compared to similar
23 estimates of an existing, calibration-free version (GCR-dyn) of the GCR that employs a
24 temporally varying dynamic scaling. Simplified annual water-balances of 327 medium and 18
25 large watersheds served as ground-truth ET values. With long-term monthly mean forcing, GCR-
26 stat (also utilizing precipitation measurements) outperforms GCR-dyn as the latter cannot fully
27 take advantage of its dynamic scaling with such data of reduced temporal variability. However,
28 in a continuous monthly simulation, GCR-dyn is on a par with GCR-stat, and especially excels in
29 reproducing long-term tendencies in annual catchment ET rates even though it does not require
30 precipitation information. The same GCR-dyn estimates were also compared to similar estimates
31 of eight other popular ET products and generally outperform all of them. For this reason, a
32 dynamic scaling of the GCR is recommended over a static one for modeling long-term behavior
33 of terrestrial ET.

34 **Key words:** land-atmosphere interactions, land evaporation, evapotranspiration, complementary
35 relationship of evaporation

36 **Article highlights:**

- 37 ■ A temporally variable dynamic scaling of the GCR yields better long-term behavior
38 than a static one.
- 39 ■ The dynamic scaling accounts for the aridity of the environment in each time step
40 thus improves land evaporation estimates.
- 41 ■ The dynamic scaling does not require precipitation information.

42

45 **1. Introduction**

46 Land surface evapotranspiration (ET) is a central component in the Earth's energy, water, and
47 carbon cycles (Wang and Dickinson, 2012; Fisher et al., 2017). Accurate ET information is
48 therefore essential for the better understanding of land-atmosphere interactions (Seneviratne et al.,
49 2006) and biosphere's water-carbon coupling (Feng et al., 2016; Biederman et al., 2016). It also
50 improves drought predictions (Pendergrass et al., 2020) and helps to find answers to water
51 resources sustainability issues (Condon et al., 2020). While the globally distributed eddy-
52 covariance flux towers have significantly contributed to our knowledge of ET across a wide range
53 of ecosystems (see a recent review by Baldocchi, 2020), the spatiotemporal variation of global ET
54 and its response to the changing climate remains highly uncertain (Muller et al., 2011; Liu et al.,
55 2016) because the estimation of long-term, spatially resolved ET is yet laden by difficulties in
56 parameterizing the biophysical processes (e.g., root water uptake, stomatal resistance and its
57 response to CO₂ concentration changes) that control ET in the current land surface models (LSMs)
58 (Ma et al., 2017; Ukkola et al., 2016) and remote sensing (RS) algorithms (Velpuri et al., 2013;
59 Vinukollu et al., 2011). In addition to possible model structural errors, the uncertainties in the
60 estimated ET can also arise from errors in their gridded vegetation (Fang et al., 2019) and soil
61 (Zheng and Yang, 2016) parameters due to the large degree of complexity/heterogeneity found in
62 terrestrial ecosystems. For example, most LSMs within the North American Land Data
63 Assimilation System phase 2 (NLDAS-2) still utilize the NOAA normalized difference vegetation
64 index data developed by Gutman and Ignatov (1998) on a 5-year-mean monthly basis without any
65 interannual variation as input (Xia et al., 2012), failing to reasonably capture the impact of

66 vegetation changes on ET. Besides, a recent sensitivity study by Li et al. (2018) demonstrated that
 67 the Noah-MP LSM cannot always capture the effect of spatial changes in forest and/or soil types
 68 on the simulated ET because of the inherent uncertainties in multiple land cover and soil texture
 69 data.

70 As an alternative, the complementary relationship (CR) (Bouchet, 1963) of evaporation inherently
 71 accounts for the dynamic feedback mechanisms found in the soil-vegetation-atmosphere interface,
 72 and thus provides a viable, robust alternative of land ET estimation relying solely on standard
 73 atmospheric forcing without the need of any soil or vegetation data. The description of the CR
 74 method applied parallels that of Ma and Szilagyi (2019) as follows in the next two paragraphs.

75 The generalized nonlinear version of the complementary relationship (GCR) by Brutsaert (2015)
 76 relates two scaled variables, $x = E_w E_p^{-1}$ and $y = E E_p^{-1}$ as

$$77 \quad y = (2 - x)x^2. \quad (1)$$

78 Here E (mm d^{-1}) is the actual, while E_p (mm d^{-1}) the potential ET rate, i.e., the evapotranspiration
 79 rate of a plot-sized wet area in a drying (i.e., not completely wet) environment, typically specified
 80 by the Penman (1948) equation as

$$81 \quad E_p = \frac{\Delta(R_n - G)}{(\Delta + \gamma)} + \frac{\gamma f_u(e^* - e)}{(\Delta + \gamma)} \quad (2)$$

82 where Δ ($\text{hPa } ^\circ\text{C}^{-1}$) is the slope of the saturation vapor pressure curve at air temperature, T ($^\circ\text{C}$),
 83 and γ the psychrometric constant ($\text{hPa } ^\circ\text{C}^{-1}$). R_n and G are net radiation at the land surface and
 84 soil heat flux into the ground, respectively (the latter is typically negligible on a daily or longer
 85 time-scale), in water equivalent of mm d^{-1} . The e^* term denotes the saturation, while $e [= e^*(T_d)]$
 86 the actual, vapor pressure of the air [hPa, their difference is called the vapor pressure deficit
 87 (VPD)]. T_d is the dew-point temperature, and f_u is a wind function, often formulated (e.g.,
 88 Brutsaert, 1982) as

89
$$f_u = 0.26(1 + 0.54u_2) \quad (3)$$

90 where u_2 (m s^{-1}) is the 2-m horizontal wind speed.

91 The so-called wet-environment ET rate, E_w (mm d^{-1}), of a well-watered land surface having a
 92 regionally significant areal extent, is specified by the Priestley-Taylor (1972) equation

93
$$E_w = \alpha \frac{\Delta(T_w)}{\Delta(T_w) + \gamma} (R_n - G) \quad (4)$$

94 The dimensionless Priestley-Taylor (PT) coefficient, α , in Eq. (4) normally attains values from the
 95 range of [1.1 – 1.32] (Morton, 1983). For large-scale model applications of gridded data Szilagyi
 96 et al. (2017) proposed a method of finding a value for α , thus avoiding the need for any calibration.

97 Very soon after the publication of the GCR, Crago et al. (2016) and Szilagyi et al. (2017)

98 introduced a necessary scaling into equation (1) by means of a time-varying wetness index, $w =$

99 $(E_p^{max} - E_p)(E_p^{max} - E_w)^{-1}$, to define the dimensionless variable, X , as $X = wx$, by which equation

100 (1) keeps its original nonlinear form, i.e.,

101
$$y = (2 - X)X^2. \quad (5)$$

102 Note that equation (4) by Priestley and Taylor (1972) was designed with measurements under wet

103 environmental conditions, therefore, Δ should be evaluated at the wet-environment air temperature,

104 T_w ($^{\circ}\text{C}$), instead of the typical, drying environment air temperature, T (Szilagyi, 2014; Szilagyi and

105 Jozsa, 2008). By making use of a mild vertical air temperature gradient (deVries 1959; Szilagyi

106 2014; Szilagyi and Jozsa 2009) observable in wet environments (as R_n is consumed predominantly

107 by the latent heat flux in the expense of the sensible one, and water representing an unusually high

108 latent heat of vaporization value found in nature), T_w can be approximated by the wet surface

109 temperature, T_{ws} ($^{\circ}\text{C}$). Note that T_{ws} may still be larger than the drying-environment air temperature,

110 T , when the air is close to saturation, but the same is not true for T_w , due to the cooling effect of

111 evaporation. In such cases the estimated value of T_w should be capped by the actual air temperature,

112 T (Szilagyi 2014; Szilagyi and Jozsa 2018). Szilagyi and Schepers (2014) demonstrated that T_{ws} is
 113 independent of the size of the wet area. T_{ws} thus can be obtained through iterations from the Bowen
 114 ratio (β) of the sensible and latent heat fluxes (Bowen, 1926) when applied over a small, plot-sized,
 115 wet patch (by the necessary assumption that the available energy for the wet patch is close to that
 116 for the drying surface) the Penman equation is valid for, i.e.,

$$117 \quad \beta = \frac{R_n - G - E_p}{E_p} \approx \gamma \frac{T_{ws} - T}{e^*(T_{ws}) - e^*(T_d)} . \quad (6)$$

118 E_p^{max} in the definition of X within equation (5) is the maximum value that E_p can achieve (under
 119 unchanging available energy for the surface) during a complete dry-out (i.e., when e_a becomes
 120 close to zero) of the environment, i.e.,

$$121 \quad E_p^{max} \approx \frac{\Delta(T_{dry})(R_n - G)}{\Delta(T_{dry}) + \gamma} + \frac{\gamma f_u e^*(T_{dry})}{\Delta(T_{dry}) + \gamma} \quad (7)$$

122 in which T_{dry} ($^{\circ}\text{C}$) is the so-achieved dry-environment air temperature. The latter can be estimated
 123 from the (isoenthalp) adiabat of an air layer in contact with the drying surface (Szilagyi, 2018a),
 124 i.e.,

$$125 \quad T_{dry} = T_{wb} + \frac{e^*(T_{wb})}{\gamma} \quad (8)$$

126 where T_{wb} ($^{\circ}\text{C}$) is the wet-bulb temperature. T_{wb} can be obtained with the help of another iteration
 127 of writing out the Bowen ratio for adiabatic changes (e.g., Szilagyi, 2014), such as

$$128 \quad \frac{\gamma(T_{wb} - T)}{e^*(T_{wb}) - e^*(T_d)} = -1 . \quad (9)$$

129 For a graphical illustration of the saturation vapor pressure curve, the different temperatures and
 130 the related ET rates defined, please, refer to Ma and Szilagyi (2019). The same source also includes
 131 a brief description of how the CR evolved into equation (5) over the past 40 years. Additionally,
 132 it plots selected historical CR functions over sample data, and explains how assigning a value of α
 133 is performed without resorting to any calibration. A sensitivity analysis of the ET rates in equation

134 (5) to their atmospheric forcing is found in Ma et al. (2019).
135 While Brutsaert et al. (2020) realized the necessity of scaling x with the help of a static aridity
136 index, Crago et al. (2016), Szilagyi et al. (2017), Szilagyi (2018a, 2018b), Szilagyi and Jozsa
137 (2018), Ma and Szilagyi (2019), Ma et al. (2019) performed one (and the same one) via a
138 dynamic wetness index. Whereas the wetness index assigns increasing values to wetter
139 environmental conditions, the aridity index does the same to drier ones. Brutsaert et al. (2020)
140 did not include this dynamic wetness index method in their study, therefore the present work was
141 initiated to fill this gap.

142

143 **2. Model applications**

144 The time-varying (thus, dynamic) scaling of x (Crago et al., 2016; Szilagyi et al., 2017) by the
145 wetness index, $w [= (E_p^{max} - E_p)(E_p^{max} - E_w)^{-1}]$, in equation (5) is necessary because the GCR of
146 Brutsaert (2015) unrealistically predicts near-zero land evaporation only when E_w in x itself
147 approaches zero. This is so because the potential evaporation rate, E_p , in the denominator of x
148 always assumes well-bounded values due to physical limits on the range of its constituents, i.e.,
149 net radiation, soil heat flux, air temperature, wind speed, and vapor pressure deficit.

150 An alternative, static scaling of x by Brutsaert et al. (2020) takes place via an adjustable
151 parameter, α_c , that acts as the PT- α value for wet environments. Since equation (4) can also be
152 written as $E_w = \alpha E_e$ where E_e is the equilibrium evaporation rate of Slatyer and McIlroy (1961),
153 thus the scaled variable, X , becomes $X = \alpha_c E_e E_p^{-1} = \alpha_c x \alpha^{-1}$. The spatially variable (but constant
154 through time at a given location) value of α_c then is related to a long-term aridity index by
155 Brutsaert et al. (2020), the latter defined as the ratio of the mean annual E_p and rain depth, and is

156 globally calibrated with the help of additional water-balance data, requiring altogether seven
157 parameters in highly non-linear equations.

158 Note that the $X = wx$ scaling by Crago et al. (2016) and Szilagyi et al. (2017) requires only the
159 forcing variables (R_n , G , T , u_2 , and VPD), without the need of external precipitation/rain data
160 which is significant as precipitation is possibly the most uncertain meteorological variable to
161 predict in climate models. It is important to mention that w changes with each value of x , unlike
162 α_c . As Szilagyi et al. (2017) demonstrated, a (temporally and spatially) constant value of the PT
163 α , necessary for x , can be set by the sole use of the forcing variables, without resorting to
164 additional water-balance data of precipitation and stream discharge, thus making the approach
165 calibration-free on a large scale (Szilagyi, 2018b; Ma et al., 2019; Ma and Szilagyi, 2019) where
166 wet-environmental conditions, necessary for setting the value of α , can likely be found. Note that
167 setting a constant value of α is also necessary for Brutsaert et al. (2020) in order to force their
168 spatially variable but temporally constant α_c values to reach a pre-determined value of about 1.3
169 under wet conditions. Despite of almost half a century of research following publication of the
170 Priestley-Taylor equation (1972), there is still no consensus about what environmental variables
171 (atmospheric, radiative, and/or surficial properties) and exactly how their spatial and temporal
172 averaging influence the value of the PT α . Until compelling information is available on these
173 variables, a spatially and temporally constant α value may suffice for modeling purposes.

174 As was found by Szilagyi (2018b), the value of the PT α depends slightly on the temporal
175 averaging of the forcing data, i.e., whether the monthly values are long-term averages or not
176 [yielding $\alpha = 1.13$ (Szilagyi et al., 2017) and 1.15 (Szilagyi, 2018b), respectively]. Therefore,
177 here it is tested if such is the case for the globally-calibrated model of Brutsaert et al. (2020).
178 Namely, if its performance is affected by similar changes (from long-term mean monthly values

179 to monthly values) in the input/forcing variables, then some caution must be exercised during its
180 routine future application and recalibration of its seven parameters may be necessary. Note that
181 besides the different scaling of x , everything is the same (including data requirements) in the two
182 GCR model versions applied here, except that Δ in E_e is evaluated at the measured air
183 temperature in Brutsaert et al. (2020) while the same in $E_w (= \alpha E_e)$ is evaluated at an estimated
184 wet-environment air temperature (Szilagyi et al., 2017) explained above.

185 Both model versions (denoted for brevity by GCR-stat and GCR-dyn, respectively) were tested
186 over the conterminous United States, first with long-term averages (1981-2010) of monthly 32-
187 km resolution North American Regional Reanalysis (NARR) (Mesinger et al., 2006) radiation
188 and 10-m wind (u_{10}) data [reduced to 2-m values via $u_2 = u_{10} (2/10)^{1/7}$ (Brutsaert, 1982)], as well
189 as with 4.2-km PRISM air, and dew-point temperature values (Daly et al., 1994) followed by a
190 continuous 37-year simulation of monthly values over the 1979-2015 period. The NARR data
191 was resampled to the PRISM grid by the nearest neighbor method. Monthly soil heat fluxes were
192 considered negligible. Evaluation of the model estimates were performed by water-balance
193 estimates of basin-representative evaporation rates (E_{wb}) with the help of United States
194 Geological Survey two- and six-digit Hydrologic Unit Code (HUC2 and HUC6) basin (Fig. 1)
195 discharge data (Q) together with basin-averaged PRISM precipitation (P) values as $E_{wb} = P - Q$,
196 either on an annual (for trend analysis) or long-term mean annual basis. The application of a
197 simplified water balance is justifiable as soil-moisture and groundwater-storage changes are
198 typically negligible over an annual (or longer) scale (Senay et al., 2011) for catchments with no
199 significant trend in the groundwater-table elevation values.

200

201 **3. Results and discussions**

202 With the long-term mean monthly data GCR-stat performed slightly, but consistently better than
203 GCR-dyn (Fig. 2), reflected best in the Nash-Sutcliffe model efficiency (NSE) and root-mean-
204 square error (RMSE) values, both models providing unbiased, basin-averaged mean annual ET
205 estimates. This outcome is not surprising as GCR-stat takes advantage of measured precipitation
206 while GCR-dyn does not.

207 When switching from long-term mean monthly forcing values to monthly values in a continuous
208 simulation, the picture, however, changes (Fig. 3). The GCR-dyn, with a slightly changed $PT-\alpha$
209 value (from 1.13 to 1.15, using the procedure of Szilagyi et al., 2017) continues to produce
210 unbiased estimates of basin-averaged mean annual evaporation values. However, the globally
211 calibrated GCR-stat model underestimates the water-balance-derived values by about 10% (i.e.,
212 relative bias, RB, is -0.09 for both basin scales) and produces reduced inter-annual variability
213 (see the horizontally elongated ‘crosses’ for the HUC2 basins in Fig. 3) in comparison with
214 GCR-dyn. Reduced model performance of GCR-stat is also apparent in the long-term linear
215 tendencies (obtained as least-squares fitted linear trends) of the basin-averaged annual
216 evaporation values (Fig. 4) by being less effective than GCR-dyn in reproducing the observed
217 linear trends in the water-balance data.

218 As on a mean-annual basis GCR-stat performs better than (with mean monthly values) or about
219 equal to (in a continuous simulation) GCR-dyn by exploiting precipitation data (which on the
220 watershed scale naturally serves as an upper bound for land ET), its weakened performance in
221 trends can only be explained by the same reliance on the long-term means of the precipitation
222 (and E_p) rates in the (therefore) static α_c values that will hinder its response to slow (decadal)
223 changes in aridity. The same problem cannot occur in GCR-dyn, since its wetness index (w) is
224 updated in each step of calculations.

225 The current GCR-dyn model has already been shown to (a) yield correlation coefficient values in
226 excess of 0.9 with local measurements of latent heat fluxes across diverse climates in China (Ma
227 et al., 2019) in spite of large differences in spatial representativeness (i.e., grid resolution vs flux
228 measurement foot-print), and; (b) outperform several popular large-scale ET products over the
229 conterminous United States (Ma and Szilagyi, 2019). These products include three land surface
230 models, namely Noah (Chen and Dudhia, 2001), VIC (Liang et al., 1994), and Mosaic (Koster
231 and Suarez, 1996); two reanalysis products: NCEP-II (Kanamitsu et al., 2002), and ERA-Interim
232 (Dee et al., 2011); another two remote-sensing based approaches: GLEAM (Miralles et al., 2011;
233 Martens et al., 2017) and PML (Leuning et al., 2008; Zhang et al., 2017); as well as a spatially
234 upscaled eddy-covariance measurement product: FLUXNET-MTE (Jung et al., 2011). In a
235 comparison with water-balance data, GCR-dyn turns out to produce even better statistics on the
236 HUC2 scale than the spatially interpolated eddy-covariance measured ET fluxes (Fig. 5), which
237 is remarkable from a calibration-free approach. GCR-dyn especially excels in the long-term
238 linear tendency estimates of the HUC2 ET rates, demonstrated by Figs. 6 and 7. As FLUXNET-
239 MTE employs several temporally static variables for its spatial interpolation method, its ability to
240 capture long-term trends is somewhat limited (Jung et al., 2011). On the contrary, the dynamic
241 scaling inherent in GCR-dyn automatically adapts to such trends and identifies them rather
242 accurately.

243 Among the different popular large-scale ET models, GCR-dyn produces multi-year mean annual
244 ET rates closest in its spatial distribution to those of FLUXNET-MTE (Fig. 8), with a spatially
245 averaged ET value almost identical (both in its spatial average and standard deviation) to that of
246 GLEAM (Fig. 8) which is a remote-sensing based approach. Note that all models of the
247 comparison (except GCR-dyn) rely on precipitation data as input, which greatly aids ET

248 estimations as on a regional scale and long-term basis, precipitation forms an upper bound for
249 terrestrial ET rates plus it may drive any required soil-moisture water-balance calculations.

250 The spatial distribution of the modeled multi-year linear ET trends is displayed in Fig. 9. Again,
251 GCR-dyn produces results closest in spatial distribution to FLUXNET-MTE in terms of the
252 statistically significant trends and to GLEAM in general. For a more detailed discussion of
253 model comparisons (including additional model descriptions), please, refer to Ma and Szilagyi
254 (2019).

255 In conclusion it can be stated that the generalized complementary relationship of evaporation
256 (Brutsaert, 2015) is a very effective tool in land ET modeling as it requires only a few, largely
257 meteorological forcing variables, and avoids the need of detailed soil-moisture and land-cover
258 information. Although attractive, as its (altogether seven) parameters have already been globally
259 pre-calibrated, the GCR model version (GCR-stat) of Brutsaert et al. (2020) may, however, not
260 perform optimally in estimating long-term tendencies in basin-wide ET rates. This is particularly
261 the case in comparison to an earlier, calibration-free version (GCR-dyn), having no pre-
262 calibrated parameter values but requiring that its sole, temporally – and spatially— constant
263 parameter (i.e., the PT coefficient) be set using the actual forcing data through a largely
264 automated method, described in Szilagyi et al. (2017). Since in a continuous monthly simulation
265 both models performed about the same, while the GCR-dyn producing better long-term
266 tendencies, a dynamic scaling of $E_w E_p^{-1}$ is recommended over a static one in future applications
267 of the generalized complementary relationship of evaporation.

268 As has been recommended before (Szilagyi, 2018b; Szilagyi ad Jozsa, 2018; Ma and Szilagyi,
269 2019), it is reiterated here that GCR-dyn due to its minimal data requirement, calibration-free
270 nature and dynamic scaling, may continue to serve as a diagnostic and benchmarking tool for

271 more complex and data intensive models of terrestrial evapotranspiration rates, including
272 calibration/verification (for past values) and reality checking (for future scenario values) of the
273 LSM-predicted ET rates of existing regional and general circulation models.

274

275 **Acknowledgements**

276 All data used in this study can be accessed from the websites as follows. NARR data:
277 www.esrl.noaa.gov/psd/data/gridded/data.narr.html. PRISM temperature, humidity and
278 precipitation: prism.oregonstate.edu/. USGS HUC2 and HUC6 runoff: [waterwatch.usgs.gov](http://waterwatch.usgs.gov/?id=wwds_runoff)
279 [/?id=wwds_runoff](http://waterwatch.usgs.gov/?id=wwds_runoff). Noah ET data: [disc.gsfc.nasa.gov/datasets/NLDAS_NOAH0125_M_V002/](http://disc.gsfc.nasa.gov/datasets/NLDAS_NOAH0125_M_V002/summary?keywords=NLDAS)
280 [summary?keywords=NLDAS](http://disc.gsfc.nasa.gov/datasets/NLDAS_NOAH0125_M_V002/summary?keywords=NLDAS). VIC ET data: [disc.gsfc.nasa.gov/datasets/NLDAS_VIC0125_](http://disc.gsfc.nasa.gov/datasets/NLDAS_VIC0125_M_V002/summary?keywords=NLDAS)
281 [M_V002/summary?keywords=NLDAS](http://disc.gsfc.nasa.gov/datasets/NLDAS_VIC0125_M_V002/summary?keywords=NLDAS). Mosaic ET data: [disc.gsfc.nasa.gov/datasets/NLDAS_](http://disc.gsfc.nasa.gov/datasets/NLDAS_MOS0125_M_V002/summary?keywords=NLDAS)
282 [MOS0125_M_V002/summary?keywords=NLDAS](http://disc.gsfc.nasa.gov/datasets/NLDAS_MOS0125_M_V002/summary?keywords=NLDAS). NCEP-II ET data:
283 www.esrl.noaa.gov/psd/data/gridded/data.ncep.reanalysis2.html. ERA-Interim ET data:
284 www.ecmwf.int/en/forecasts/datasets/reanalysis-datasets/era-interim. GLEAM ET data:
285 <http://gleam.eu/#home>. PML ET data: [data.csiro.au/dap/landingpage?pid=csiro:17375&v=](http://data.csiro.au/dap/landingpage?pid=csiro:17375&v=%202&d=true)
286 [%202&d=true](http://data.csiro.au/dap/landingpage?pid=csiro:17375&v=%202&d=true). FLUXNET-MTE ET data: [climatedataguide.ucar.edu/climate-data/fluxnet-mte-](http://climatedataguide.ucar.edu/climate-data/fluxnet-mte-multi-tree-ensemble)
287 [multi-tree-ensemble](http://climatedataguide.ucar.edu/climate-data/fluxnet-mte-multi-tree-ensemble). The GCR-dyn modeled ET rates and the HUC2- and HUC6-averaged E_{wb} ,
288 P , Q , data are available from <https://digitalcommons.unl.edu/natrespapers/986/>. This research
289 was supported by BME-Water Sciences and Disaster Prevention FIKP grant of EMMI (BME
290 FIKP-VIZ).

291

292

293 REFERENCES

- 294 Baldocchi, D. D., 2020: How eddy covariance flux measurements have contributed to our
295 understanding of Global Change Biology. *Global Change Biology*, 26, 242-260,
296 <https://doi.org/10.1111/gcb.14807>.
- 297 Bouchet, R. J., 1963: Evapotranspiration réelle et potentielle, signification climatique.
298 *International Association of Scientific Hydrology*, 62, 134-142.
- 299 Bowen, I. S., 1926: The ratio of heat losses by conduction and by evaporation from any water
300 surface. *Physical Review*, 27, 779-787.
- 301 Brutsaert, W., 1982: *Evaporation into the atmosphere: Theory, history and applications*.
302 Dordrecht, Holland: D. Reider, <https://doi.org/10.1007/978-94-017-1497-6>.
- 303 Brutsaert, W., 2015: A generalized complementary principle with physical constraints for land-
304 surface evaporation. *Water Resources Research*, 51, 8087-8093, [https://doi.org/10.1002/](https://doi.org/10.1002/2015WR017720)
305 [2015WR017720](https://doi.org/10.1002/2015WR017720).
- 306 Brutsaert, W., L. Cheng, and L. Zhang, 2020: Spatial distribution of global landscape
307 evaporation in the early twenty first century by means of a generalized complementary
308 approach. *Journal of Hydrometeorology*, 21, 287-298, [https://doi.org/10.1175/JHM-D-](https://doi.org/10.1175/JHM-D-19-0208.1)
309 [19-0208.1](https://doi.org/10.1175/JHM-D-19-0208.1).
- 310 Chen, F., and J. Dudhia, 2001: Coupling an advanced land surface-hydrology model with the
311 Penn State-NCAR MM5 modeling system. Part I: Model implementation and sensitivity.
312 *Monthly Weather Review*, 129(4), 569–585,
313 [https://doi.org/10.1175/1520-0493\(2001\)1292.0.CO;2](https://doi.org/10.1175/1520-0493(2001)1292.0.CO;2).

314 Condon, L. E., A. L. Atchley, and R. M. Maxwell, 2020: Evapotranspiration depletes
315 groundwater under warming over the contiguous United States. *Nature Communications*,
316 *11*, 873, <https://doi.org/10.1038/s41467-020-14688-0>.

317 Crago, R., J. Szilagyi, R. Qualls, and J. Huntington, 2016: Rescaling the complementary
318 relationship for land surface evaporation. *Water Resources Research*, *52*, 8461-8471,
319 <https://doi.org/10.1002/2016WR019753>.

320 Daly, C., R. P. Neilson, and D. L. Phillips, 1994: A statistical topographic model for mapping
321 climatological precipitation over mountainous terrain. *Journal of Applied Meteorology*,
322 *33*, 140–158.

323 Dee, D. P., S. M. Uppala, A. J. Simmons, P. Berrisford, P. Poli, S. Kobayashi et al., 2011: The
324 ERA-Interim reanalysis: Configuration and performance of the data assimilation system.
325 *Quarterly Journal of the Royal Meteorological Society*, *137*(656), 553–597,
326 <https://doi.org/10.1002/qj.828>.

327 deVries, D. A., 1959: The influence of irrigation on the energy balance and the climate near the
328 ground. *Journal of Meteorology*, *16*, 256-270.

329 Fang, H., F. Baret, S. Plummer, and G. Schaepman-Strub, 2019: An overview of global leaf area
330 Index (LAI): Methods, products, validation, and applications. *Reviews of Geophysics*, *57*,
331 739-799, <https://doi.org/10.1029/2018rg000608>.

332 Feng, X., B. Fu, S. Piao, S. Wang, P. Ciais, Z. Zeng, Y. Lü, Y. Zeng, Y. Li, X. Jiang, and B. Wu,
333 2016: Revegetation in China's Loess Plateau is approaching sustainable water resource
334 limits. *Nature Climate Change*, *6*, 1019-1022, <https://doi.org/10.1038/nclimate3092>.

335 Fisher, J. B., F. Melton, E. Middleton, C. Hain, M. Anderson, R. Allen, M. F. McCabe, S. Hook,
336 D. Baldocchi, P. A. Townsend, A. Kilic, K. Tu, D. D. Miralles, J. Perret, J.-P. Lagouarde,
337 D. Waliser, A. J. Purdy, A. French, D. Schimel, J. S. Famiglietti, G. Stephens, and E. F.
338 Wood, 2017: The future of evapotranspiration: Global requirements for ecosystem
339 functioning, carbon and climate feedbacks, agricultural management, and water
340 resources. *Water Resources Research*, 53, 2618-2626,
341 <https://doi.org/10.1002/2016wr020175>.

342 Gutman, G., and A. Ignatov, 1998: The derivation of green vegetation fraction from
343 NOAA/AVHRR data for use in numerical weather prediction models. *International*
344 *Journal of Remote Sensing*, 19, 1533-1543.

345 Jung, M., M. Reichstein, H. A. Margolis, A. Cescatti, A. D. Richardson, M. A. Arain et al., 2011:
346 Global patterns of land-atmosphere fluxes of carbon dioxide, latent heat, and sensible
347 heat derived from eddy covariance, satellite, and meteorological observations. *Journal of*
348 *Geophysical Research*, 116, G00J07, <https://doi.org/10.1029/2010jg001566>.

349 Kanamitsu, M., W. Ebisuzaki, J. Woollen, S.-K. Yang, J. J. Hnilo, M. Fiorino, and G. L. Potter,
350 2002: NCEP-DOE AMIP-II Reanalysis (R- 2). *Bulletin of the American Meteorological*
351 *Society*, 83(11), 1631–1644, <https://doi.org/10.1175/BAMS-83-11>.

352 Koster, R., and M. Suarez, 1996: Energy and water balance calculations in the Mosaic LSM.
353 Report, 58 pp. Goddard Space Flight Center, National Aeronautics and Space
354 Administration, Greenbelt, Maryland.

355 Leuning, R., Y. Q. Zhang, A. Rajaud, H. Cleugh, and K. Tu, 2008: A simple surface conductance
356 model to estimate regional evaporation using MODIS leaf area index and the

357 Penman-Monteith equation. *Water Resources Research*, 44, W10419,
358 <https://doi.org/10.1029/2007WR006562>.

359 Li, J., F. Chen, G. Zhang, M. Barlage, Y. Gan, Y. Xin, and C. Wang, 2018: Impacts of land
360 cover and soil texture uncertainty on land model simulations over the Central Tibetan
361 Plateau. *Journal of Advances in Modeling Earth Systems*, 10, 2121-2146,
362 <https://doi.org/10.1029/2018MS001377>.

363 Liang, X., D. P. Lettenmaier, E. F. Wood, and S. J. Burges, 1994: A simple hydrologically based
364 model of land surface water and energy fluxes for general circulation models. *Journal of*
365 *Geophysical Research*, 99(D7), 14,415–14,428, <https://doi.org/10.1029/94JD00483>.

366 Liu, W., L. Wang, J. Zhou, Y. Li, F. Sun, G. Fu, X. Li, and Y.-F. Sang, 2016: A worldwide
367 evaluation of basin-scale evapotranspiration estimates against the water balance method.
368 *Journal of Hydrology*, 538, 82-95, <https://doi.org/10.1016/j.jhydrol.2016.04.006>.

369 Ma, N., and J. Szilagyi, 2019: The complementary relationship (CR) of evaporation: a
370 calibration-free diagnostic and benchmarking tool for large-scale terrestrial
371 evapotranspiration modeling. *Water Resources Research*, 55(8), 7246-7274,
372 <https://doi.org/10.1029/2019WR024867>.

373 Ma, N., G.-Y. Niu, Y. Xia, X. Cai, Y. Zhang, Y. Ma, and Y. Fang, 2017: A systematic evaluation
374 of Noah-MP in simulating land-atmosphere energy, water, and carbon exchanges over the
375 continental United States. *Journal of Geophysical Research: Atmospheres*, 122(22),
376 12245-12268, <https://doi.org/10.1002/2017JD027597>.

377 Ma, N., J. Szilagyi, Y. Zhang, and W. Liu, 2019: Complementary-relationship-based modeling
378 of terrestrial evapotranspiration across China during 1982-2012: Validations and

379 spatiotemporal analyses. *Journal of Geophysical Research: Atmospheres*, 124,
380 <https://doi.org/10.1029/2018JD029850>.

381 Martens, B., D. G. Miralles, H. Lievens, R. van der Schalie, R. A. M. de Jeu, D.
382 Fernández-Prieto et al., 2017: GLEAM v3: Satellite- based land evaporation and
383 root-zone soil moisture. *Geoscientific Model Development*, 10(5), 1903–1925,
384 <https://doi.org/10.5194/gmd-10-1903-2017>.

385 Mesinger, F., G. DiMego, E. Kalnay, K. Mitchell, P. C. Shafran, W. Ebisuzaki, D. Jovic, J.
386 Woollen, E. Rogers, E. H. Berbery, M. B. Ek, Y. Fan, R. Grumbine, W. Higgins, H. Li,
387 Y. Lin, G. Manikin, D. Parrish, and W. Shi, 2006: North American regional reanalysis.
388 *Bulletin of the American Meteorological Society*, 87, 343–360.

389 Miralles, D. G., T. R. H. Holmes, R. A. M. De Jeu, J. H. Gash, A. G. C. A. Meesters, and A. J.
390 Dolman, 2011: Global land-surface evaporation estimated from satellite-based
391 observations. *Hydrology and Earth System Sciences*, 15(2), 453–469,
392 <https://doi.org/10.5194/hess-15-453-2011>.

393 Morton, F. I., 1983: Operational estimates of areal evapotranspiration and their significance to the
394 science and practice of hydrology. *Journal of Hydrology*, 66, 1-76.

395 Mueller, B., S. I. Seneviratne, C. Jimenez, T. Corti, M. Hirschi, G. Balsamo, P. Ciais, P.
396 Dirmeyer, J. B. Fisher, Z. Guo, M. Jung, F. Maignan, M. F. McCabe, R. Reichle, M.
397 Reichstein, M. Rodell, J. Sheffield, A. J. Teuling, K. Wang, E. F. Wood, and Y. Zhang,
398 2011: Evaluation of global observations-based evapotranspiration datasets and IPCC
399 AR4 simulations. *Geophysical Research Letters*, 38,
400 <https://doi.org/10.1029/2010gl046230>.

401 Pendergrass, A. G., G. A. Meehl, R. Pulwarty, M. Hobbins, A. Hoell, A. AghaKouchak, C. J. W.
402 Bonfils, A. J. E. Gallant, M. Hoerling, D. Hoffmann, L. Kaatz, F. Lehner, D. Llewellyn,
403 P. Mote, R. B. Neale, J. T. Overpeck, A. Sheffield, K. Stahl, M. Svoboda, M. C. Wheeler,
404 A. W. Wood, and C. A. Woodhouse, 2020: Flash droughts present a new challenge for
405 subseasonal-to-seasonal prediction. *Nature Climate Change*, *10*, 191-199,
406 <https://doi.org/10.1038/s41558-020-0709-0>.

407 Penman, H. L., 1948: Natural evaporation from open water, bare soil and grass. *Proceedings of*
408 *the Royal Society A: Mathematical, Physical and Engineering Sciences*, *193*, 120-145,
409 <https://doi.org/10.1098/rspa.1948.0037>.

410 Priestley, C. H. B., and R. J. Taylor, 1972: On the assessment of surface heat flux and
411 evaporation using large-scale parameters. *Monthly Weather Review*, *100*(2), 81-92.

412 Seneviratne, S. I., D. Lüthi, M. Litschi, and C. Schär, 2006: Land-atmosphere coupling and
413 climate change in Europe. *Nature*, *443*, 205-209.

414 Senay, G. B., Leake, S., Nagler, P. L., Artan, G., Dickinson, J., Cordova, J. T., and E. P. Glenn,
415 2011: Estimating basin scale evapotranspiration (ET) by water balance and remote
416 sensing methods. *Hydrological Processes*, *25*(26), 4037–4049, [https://doi.org/10.1002/](https://doi.org/10.1002/hyp.8379)
417 [hyp.8379](https://doi.org/10.1002/hyp.8379).

418 Slatyer, R. O., and I. C. McIlroy, 1961: *Practical Microclimatology*. CSIRO, Melbourne, 564
419 Australia, 310 pp.

420 Szilagyi, J., 2014: Temperature corrections in the Priestley-Taylor equation of evaporation.
421 *Journal of Hydrology*, *519*, 455-464, <https://doi.org/10.1016/j.jhydrol.2014.07.040>.

422 Szilagyi, J., 2018a: Anthropogenic hydrological cycle disturbance at a regional scale: State-wide
423 evapotranspiration trends (1979–2015) across Nebraska, USA. *Journal of Hydrology*,
424 557, 600-612, <https://doi.org/10.1016/j.jhydrol.2017.12.062>.

425 Szilagyi, J., 2018b: A calibration-free, robust estimation of monthly land surface
426 evapotranspiration rates for continental-scale hydrology. *Hydrological Research*, 49(3),
427 648-657, <https://doi.org/10.2166/nh.2017.078>.

428 Szilagyi, J., and J. Jozsa, 2008: New findings about the complementary relationship based
429 evaporation estimation methods. *Journal of Hydrology*, 354, 171-186,
430 <https://doi.org/10.1016/j.jhydrol.2008.03.008>.

431 Szilagyi, J., and J. Jozsa, 2009: Analytical solution of the coupled 2-D turbulent heat and vapor
432 transport equations and the complementary relationship of evaporation. *Journal of*
433 *Hydrology*, 372, 61-67.

434 Szilagyi, J., and J. Jozsa, 2018: Evapotranspiration trends (1979-2015) in the Central Valley of
435 California, USA: Contrasting tendencies during 1981-2007. *Water Resources Research*,
436 54, <https://doi.org/10.1029/2018WR022704>.

437 Szilagyi, J., and A. Schepers, 2014: Coupled heat and vapor transport: the thermostat effect of a
438 freely evaporating land surface. *Geophysical Research Letters*, 41, 435-441,
439 <https://doi.org/10.1002/2013GL058979>.

440 Szilagyi, J., R. Crago R., and R. J. Qualls, 2017: A calibration-free formulation of the
441 complementary relationship of evaporation for continental-scale hydrology. *Journal of*
442 *Geophysical Research: Atmospheres*, 122, 264-278,
443 <https://doi.org/10.1002/2016jd025611>.

444 Velpuri, N. M., G. B. Senay, R. K. Singh, S. Bohms, and J. P. Verdin, 2013: A comprehensive
445 evaluation of two MODIS evapotranspiration products over the conterminous United
446 States: Using point and gridded FLUXNET and water balance ET. *Remote Sensing of*
447 *Environment*, 139, 35-49, <https://doi.org/10.1016/j.rse.2013.07.013>.

448 Vinukollu, R. K., E. F. Wood, C. R. Ferguson, and J. B. Fisher, 2011: Global estimates of
449 evapotranspiration for climate studies using multi-sensor remote sensing data: Evaluation
450 of three process-based approaches. *Remote Sensing of Environment*, 115, 801-823,
451 <https://doi.org/10.1016/j.rse.2010.11.006>.

452 Wang, K., and R. E. Dickinson, 2012: A review of global terrestrial evapotranspiration:
453 Observation, modeling, climatology, and climatic variability. *Reviews of Geophysics*, 50,
454 <https://doi.org/10.1029/2011rg000373>.

455 Xia, Y., K. Mitchell, M. Ek, J. Sheffield, B. Cosgrove, E. Wood, L. Luo, C. Alonge, H. Wei, J.
456 Meng, B. Livneh, D. Lettenmaier, V. Koren, Q. Duan, K. Mo, Y. Fan, and D. Mocko,
457 2012: Continental-scale water and energy flux analysis and validation for the North
458 American Land Data Assimilation System project phase 2 (NLDAS-2): 1.
459 Intercomparison and application of model products. *Journal of Geophysical Research:*
460 *Atmospheres*, 117, <https://doi.org/10.1029/2011jd016048>.

461 Zhang, Y., F. H. S. Chiew, J. Peña-Arancibia, F. Sun, H. Li, and R. Leuning, 2017: Global
462 variation of transpiration and soil evaporation and the role of their major climate drivers.
463 *Journal of Geophysical Research: Atmospheres*, 122, 6868–6881,
464 <https://doi.org/10.1002/2017JD027025>.

465 Zheng, H., and Z.-L. Yang, 2016: Effects of soil-type datasets on regional terrestrial water cycle
466 simulations under different climatic regimes. *Journal of Geophysical Research:*
467 *Atmospheres*, 121, 14387-14402, <https://doi.org/10.1002/2016JD025187>.

468

469

470

471

472

473

474

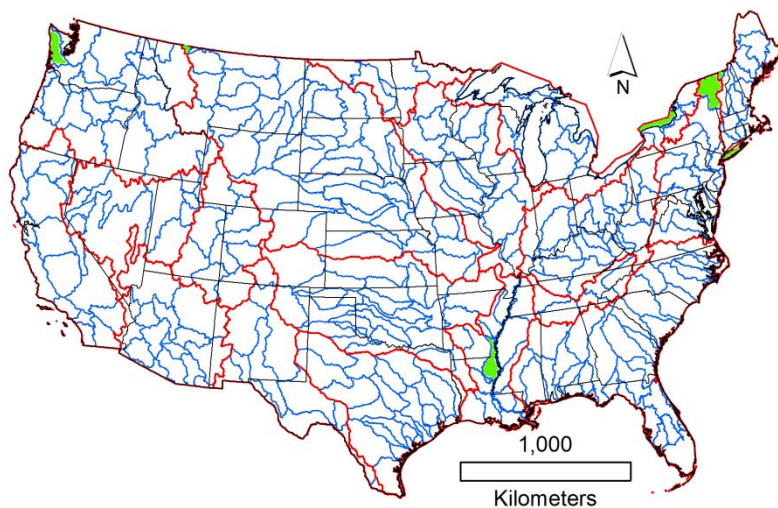
475

476

477

478

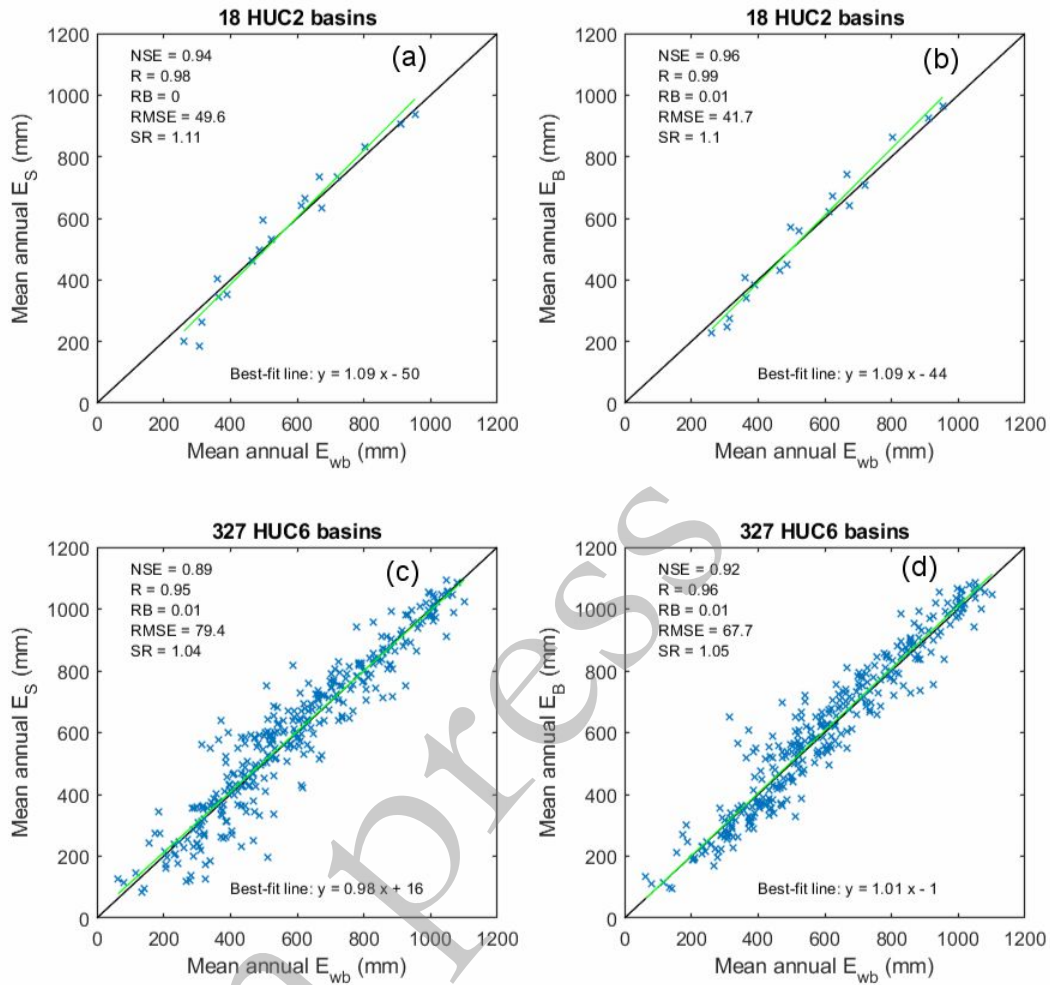
in press



479

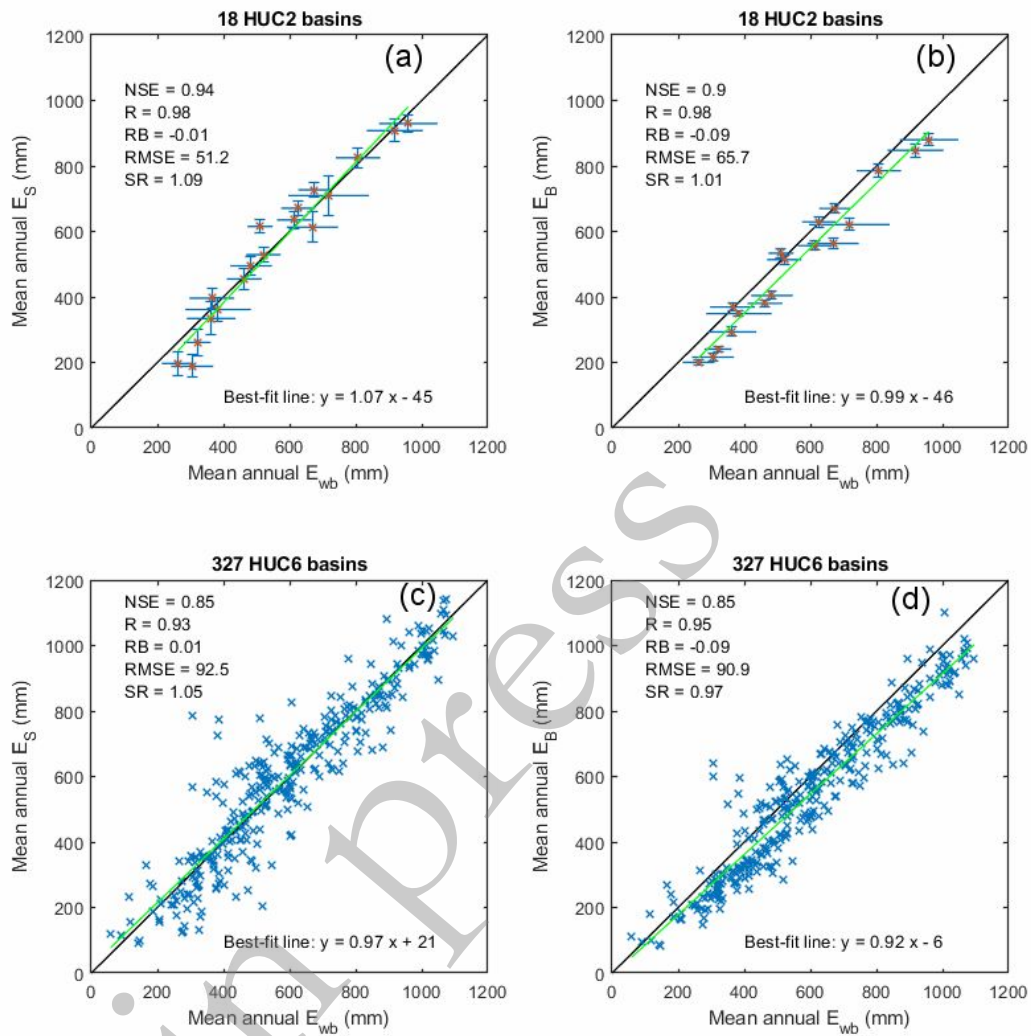
480 Fig. 1. Distribution of the 18 HUC2 (outlined in red) and 334 HUC6 basins across the
481 conterminous United States. Seven HUC6 basins, marked by green, yielded outlying water-
482 balance-derived evaporation estimates and were left out of model comparisons.

in press



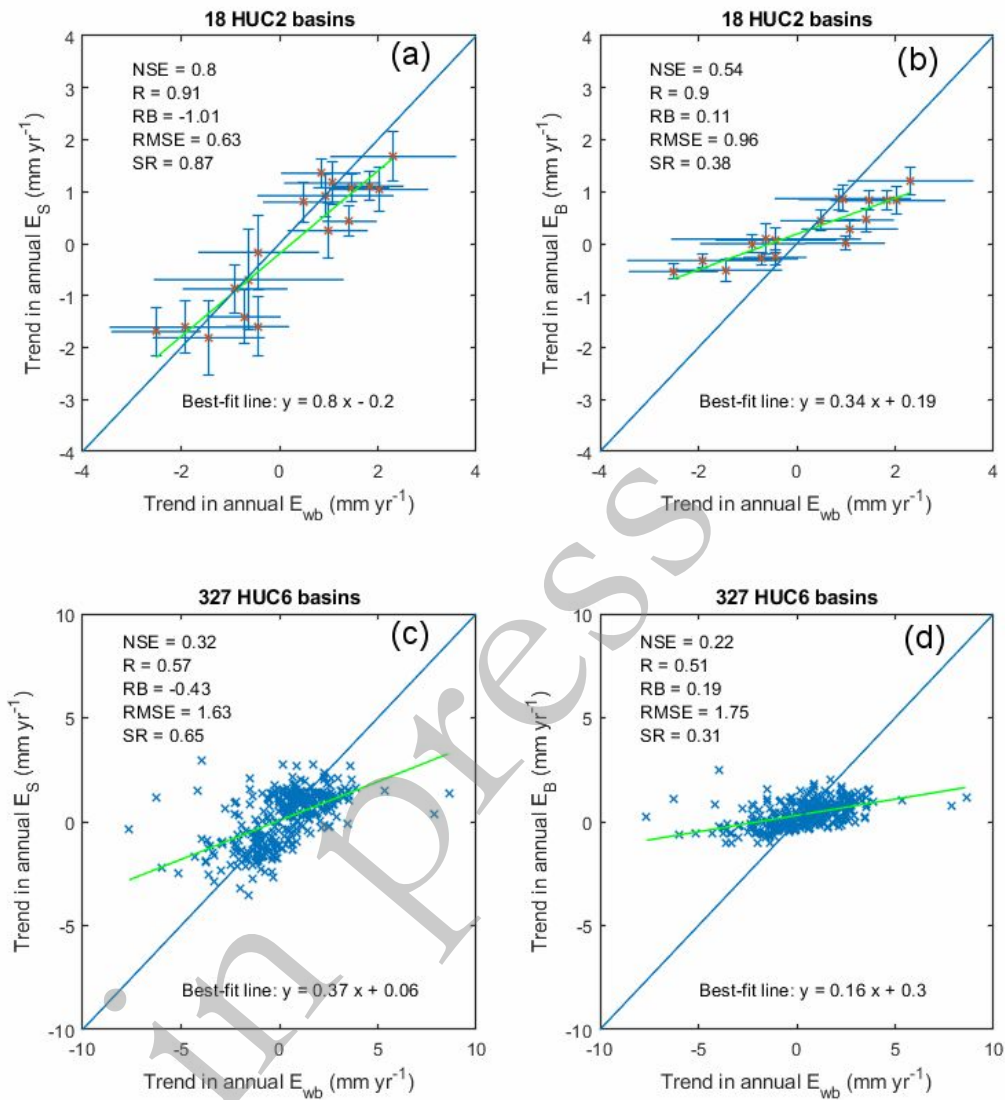
484

485 Fig. 2. Regression plots of model estimates [E_S (a, c) from GCR-dyn; E_B (b, d) from GCR-stat)
 486 against water-balance (E_{wb}) evaporation rates. Long-term mean (1981-2010) monthly values
 487 served as model forcing. $\alpha = 1.13$ in GCR-dyn (a, c). NSE: Nash-Sutcliffe model efficiency; R:
 488 linear correlation coefficient; RB: relative bias; RMSE: root-mean-square error (mm); SR: ratio
 489 of standard deviations of the mean annual model and water-balance values.



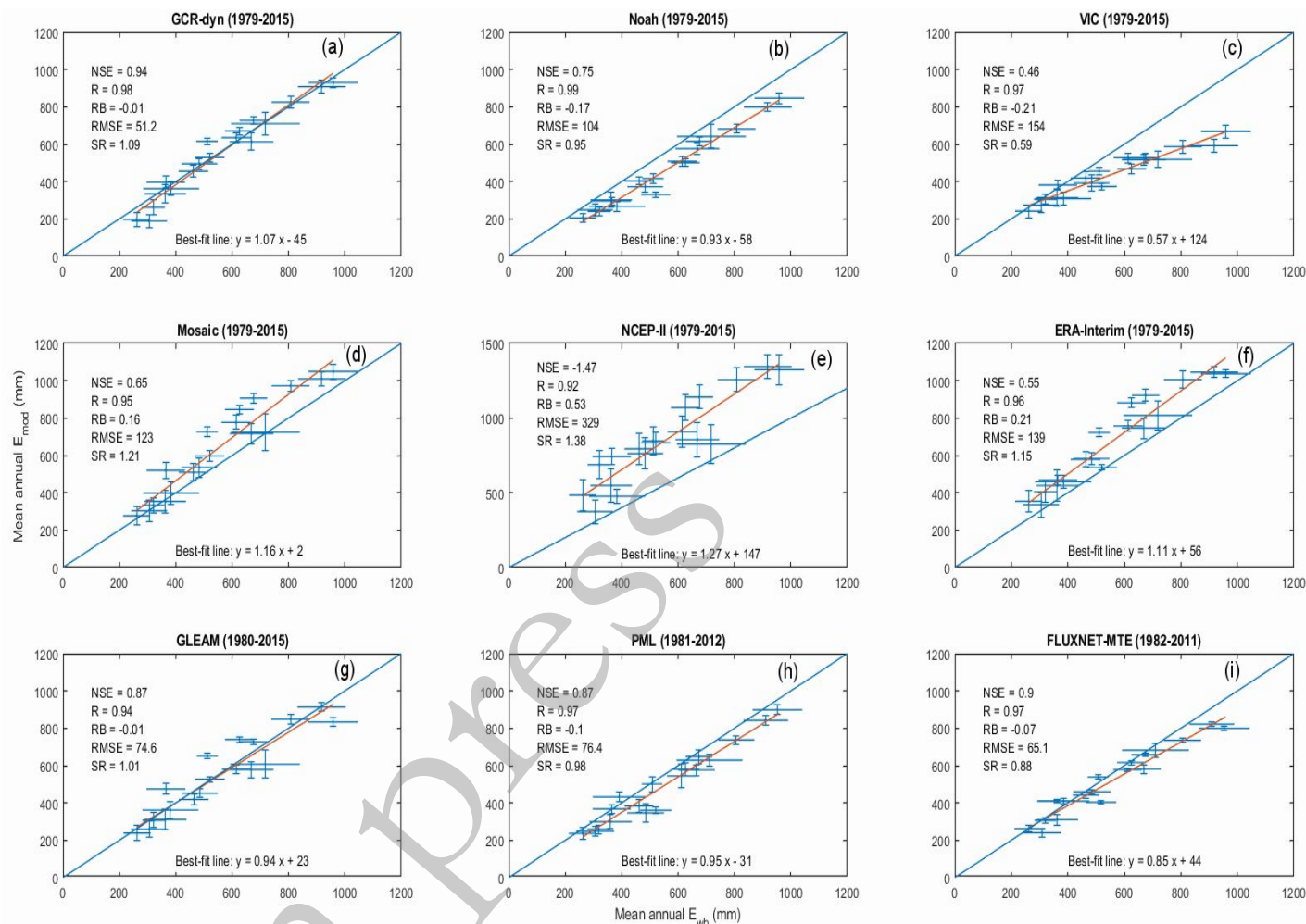
491

492 Fig. 3. Regression plots of model estimates [E_S (a, c) from GCR-dyn; E_B (b, d) from GCR-stat]
 493 against water-balance (E_{wb}) evaporation rates. Monthly (1979-2015) values served as model
 494 forcing for the continuous simulation of monthly evaporation rates. $\alpha = 1.15$ in GCR-dyn (a, c).
 495 The vertical and horizontal bars represent the standard deviation of the annual modeled and
 496 water-balance HUC2 values, respectively. The large number of data points hinders a similar plot
 497 for the HUC6 values.



499

500 Fig. 4. Regression plots of the linear trends (1979-2015) in annual modeled [E_S (a, c) from GCR-
 501 dyn; E_B (b, d) from GCR-stat] and water-balance values. The vertical and horizontal bars
 502 represent the standard error in the trend-value estimates for the modeled and water-balance
 503 HUC2 values (a, b), respectively. The large number of data points hinders a similar plot of the
 504 HUC6 values (c, d). RMSE now is in mm yr^{-1} .



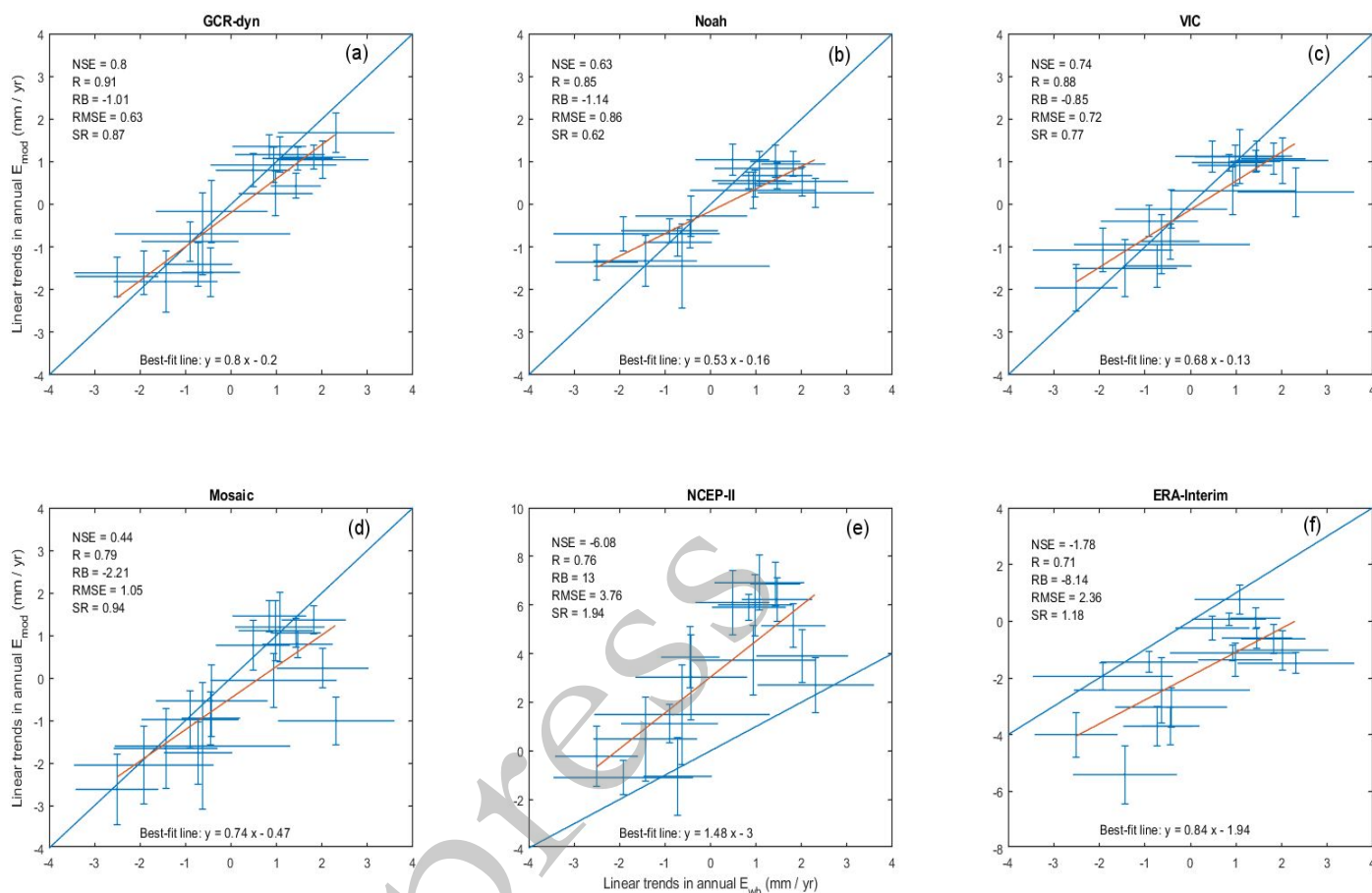
506

507 Fig. 5. Regression plots of the HUC2-averaged multiyear mean annual ET rates (E_{mod}) of GCR-
 508 dyn (a) and eight other (b-i) popular large-scale ET models against the simplified water-balance
 509 (E_{wb}) estimates. Temporal averaging follows the availability of data displayed in parenthesis for
 510 each product. The length of the whiskers denotes the standard deviation of the HUC2-basin
 511 averaged annual ET values. The long blue line represents a 1:1 relationship, while the least-
 512 squares fitted linear relationships are shown in maroon color (after Ma and Szilagyi, 2019).

513

514

515



516

517 Fig. 6. Regression plots of the linear trend values (mm yr^{-1}) in modeled HUC2-averaged annual
518 ET sums (E_{mod}) against those in E_{wb} over 1979–2015. The length of the whiskers denotes the
519 standard error in the estimated slope value. The long blue line represents a 1:1 relationship, while
520 the least-squares fitted linear relationships are shown in maroon color (after Ma and Szilagyi,
521 2019).

522

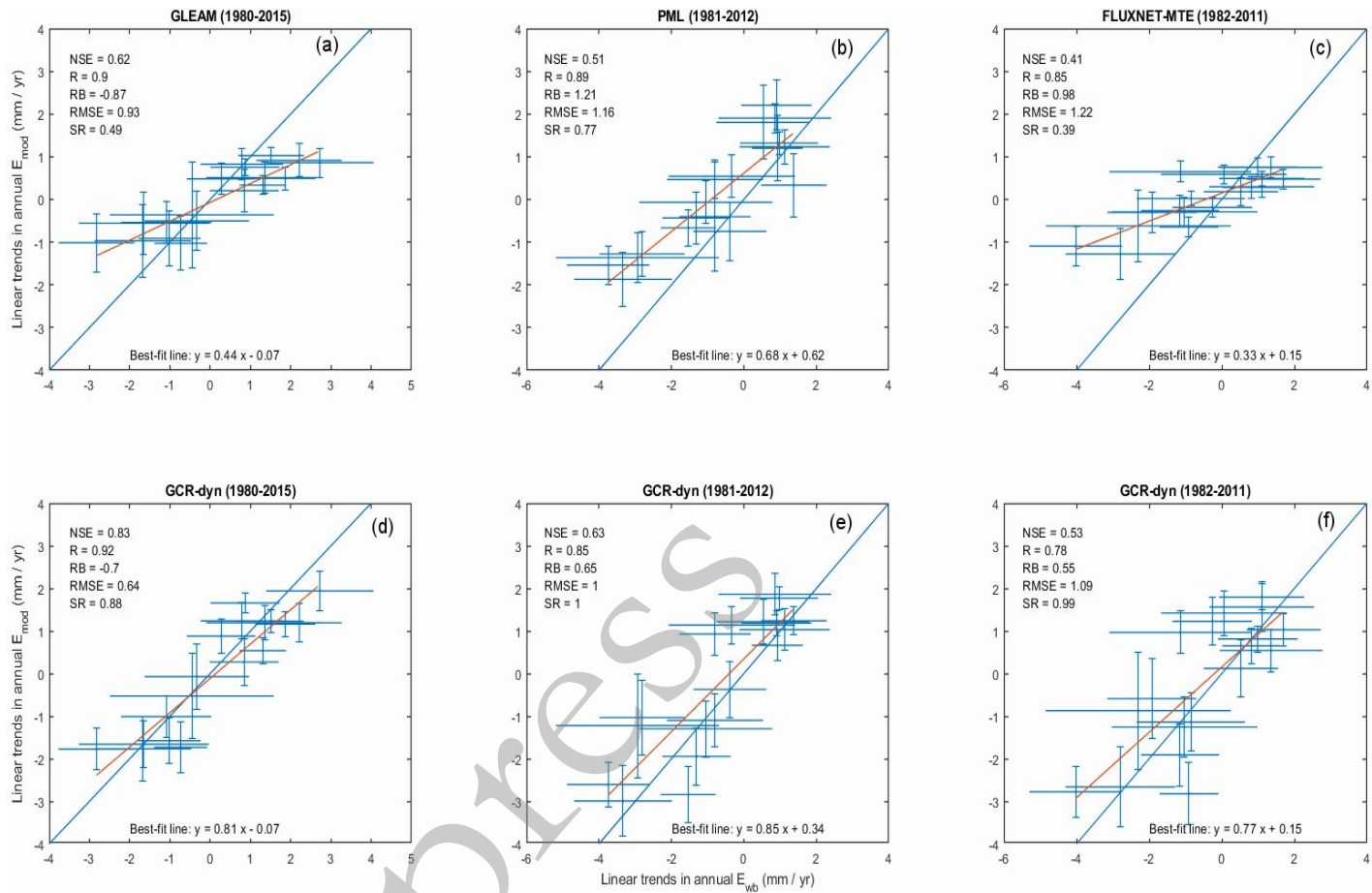
523

524

525

526

527

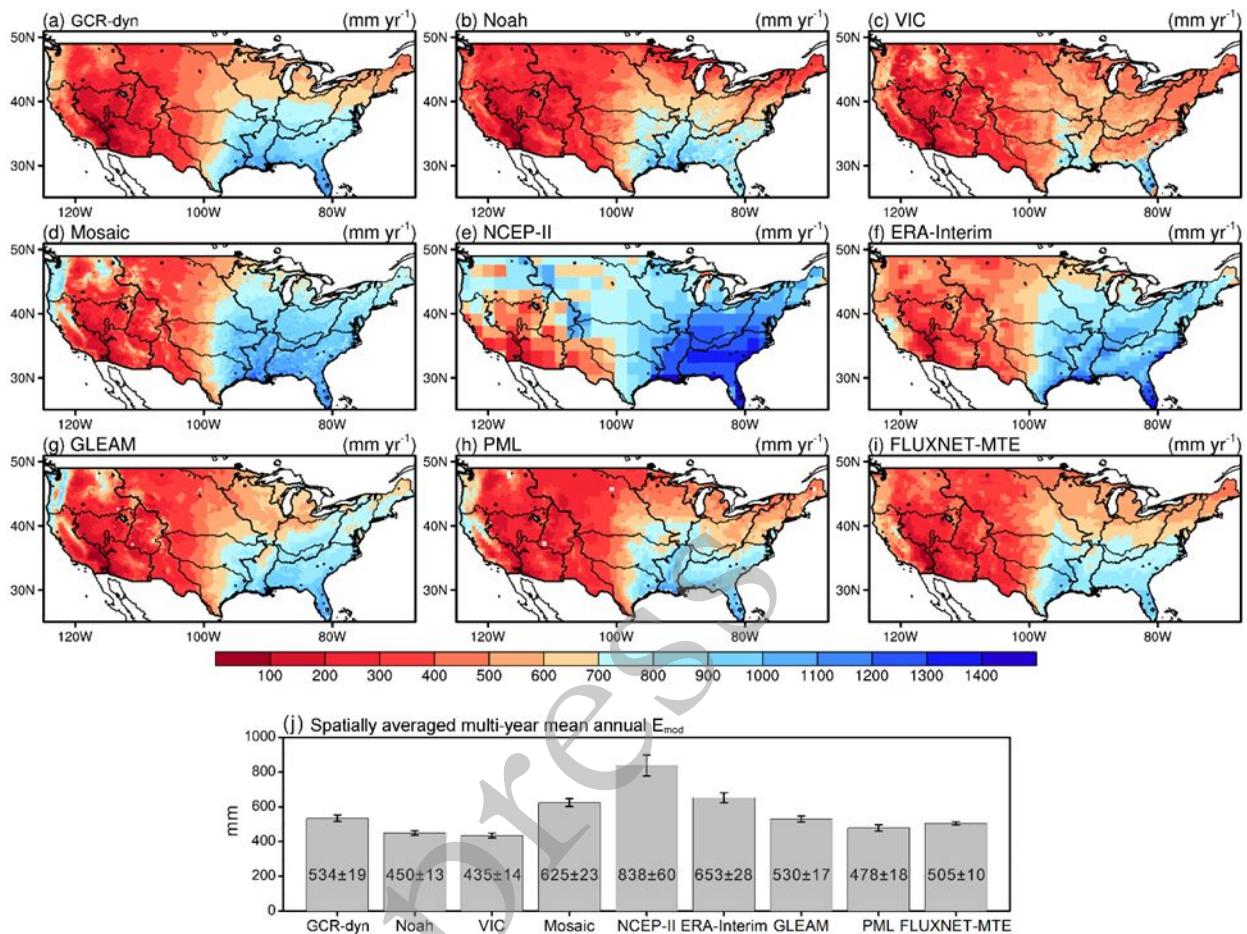


528

529 Fig. 7. Regression plots of the linear trend values (mm yr^{-1}) in GLEAM-, PML-, and
530 FLUXNET-MTE-modeled (a-c) HUC2-averaged annual ET sums (E_{mod}) against those in E_{wb}
531 over the different model periods (shown in parenthesis). For comparison, regressions for the
532 GCR-dyn ET values over the same periods are also displayed (d-f). The length of the whiskers
533 denotes the standard error in the estimated slope value. The long blue line represents a 1:1
534 relationship, while the least-squares fitted linear relationships are shown in maroon color (after
535 Ma and Szilagyi, 2019).

536

537



539

540 Fig. 8. Spatial distribution of the multiyear (1979-2015) mean annual ET (mm) rates (E_{mod}) by
 541 GCR-dyn and eight other popular large-scale ET models (a-i) and their spatially averaged (j)
 542 values, plus/minus standard deviations (after Ma and Szilagyi, 2019). The 18 HUC2 basins are
 543 also outlined.

544

545

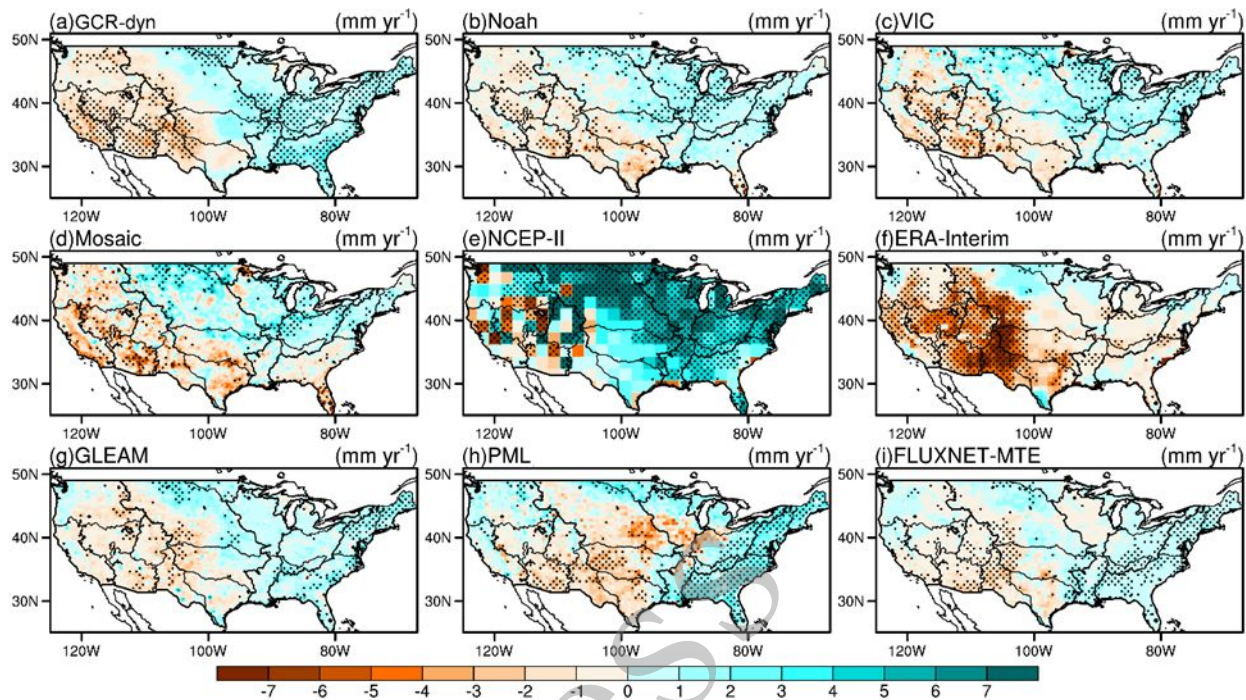
546

547

548

549

550



551

552 Fig. 9. Spatial distribution of the linear tendencies (mm yr^{-1}) in annual ET sums of GCR-dyn and
553 eight other popular large-scale ET products. The stippling denotes trends that are statistically
554 significant ($p < 5\%$) in the Student's t-test (after Ma and Szilagyi, 2019).